Official journal of the JHL 2689-9620
www.light-am.com

Article Open Access

‘Plug-and-play’ plasmonic metafibers for ultrafast fibre lasers

Lei Zhang[1,2,3], Huiru Zhang[4], Ni Tang[2,3], Xiren Chen[4], Fengjiang Liu[2,3], Xiaoyu Sun[1,2,3], Hongyan Yu[2,3], Xinyu Sun[2,3], Qiannan Jia[1,2,3], Boqu Chen[1,2,3], Benoit Cluzel[5], Philippe Grelu[5], Aurelien Coillet[5], Feng Qiu[2,3], Lei Ying[6], Wei E. I. Sha[7], Xiaofeng Liu[8], Jianrong Qiu[9], Ding Zhao[2,3], Wei Yan[2,3], Duanduan Wu[4,*], Xiang Shen[4,*], Jiyong Wang[2,3,*] and Min Qiu[2,3,*]

Abstract

Metafibers expand the functionalities of conventional optical fibres to unprecedented nanoscale light manipulations by integrating metasurfaces on the fibre tips, becoming an emerging light-coupling platform for both the nanoscience and fibre optics communities. Current metafibers remain proof-of-concept demonstrations that mostly explore isolated bare fibres owing to the lack of standard interfaces with universal fibre networks. Here, we develop methodologies for fabricating well-defined plasmonic metasurfaces directly on the end facets of commercial single -mode fibre jumpers using standard planar technologies and provide the first demonstration of their practical applications in the nonlinear plasmonic regime. Featuring plug-and-play connections with fibre circuitry and arbitrary metasurface landscapes, the metafibers with tunable plasmonic resonances are implemented into fibre laser cavities, yielding all-fibre sub-picosecond (minimum 513 fs) soliton mode locked lasers at optical wavelengths of 1.5 μm and 2 μm, demonstrating their unusual polarimetric nonlinear transfer functions and superior saturation absorption responses. The nanofabrication process flow is compatible with existing cleanroom technologies, offering metafibers an avenue to become a regular member of functionalised fibre components. This work paves the way toward the next generation of ultrafast lasers, optical frequency combs, and ultracompact ‘all-in-fibre’ optical systems.

Keywords: Nonlinear plasmonics, Metasurfaces, Metafibers, Fibre lasers, Saturable absorption

Introduction

Plasmonic metasurfaces are formed by artificially patterning subwavelength nanostructures in two-dimensional (2D) arrays[1–4]. Their plasmonic resonances are intentionally designed by altering the spatial distribution and orientation of unit cells to improve the interactions of the impinging light by enhancing the absorption and scattering cross sections, both in linear and nonlinear optical regimes[5–10]. Indeed, the nonlinear absorption of plasmonic metasurfaces has attracted increasing interest in recent years for state-of-the-art applications, including frequency conversion[6,9], neuromorphic circuits[11–13], and ultrashort laser pulse generation[14,15]. Pioneering studies

Correspondence: Duanduan Wu (wuduanduan@nbu.edu.cn) or Xiang shen (shenxiang@nbu.edu.cn) or Jiyong Wang (wangjiyong@westlake.edu.cn) or Min Qiu (qiumin@westlake.edu.cn)
[1]College of Information Science and Electronic Engineering, Zhejiang University, Hangzhou 310027, China
[2]Key Laboratory of 3D Micro/Nano Fabrication and Characterization of Zhejiang Province, School of Engineering, Westlake University, 18 Shilongshan Road, Hangzhou 310024, Zhejiang Province, China
Full list of author information is available at the end of the article.
These authors contributed equally: Lei Zhang, Huiru Zhang

employed plasmonic metasurfaces as saturable absorbers (SAs) in a fibre laser, leading to soliton mode locking[15,16]. Owing to their well-defined shapes, sizes, and orientations, the metasurface SA demonstrated the superiority of tunable modulation depths and strong bonding to the plasmonic nature, outperforming the colloidal nanoparticles intensively used in fibre lasers[14,17,18]. However, such metasurface SAs were realised solely in a free-space coupled fibre laser cavity, regardless of the practical integration requirements and more in-depth physical mechanisms of saturable absorption.

Plasmonic metasurfaces are routinely fabricated on planar wafers, thus maintaining a large compatibility with conventional semiconductor technologies. Advanced nonplanar substrates involving atomic force microscope tips, carbon nanotubes, and silver nanowires have been explored in recent years using state-of-the-art nanofabrication methods[19,20], which are exclusively limited to scientific demonstrations. Optical fibre tips that combine fibre optics and planar technologies are emerging as one of the most promising light-coupling platforms for both scientific and industrial communities[21,22]. Integrating plasmonic metasurfaces on optical fibre tips to form metafibers expands the functionalities of an ordinary optical fibre to nanoscale manipulation of light, yielding a variety of advanced applications such as planar waveshaping[21,23], super-resolution imaging[24], and ultracompact sensing[25–27]. Several strategies are applied for fabricating metafibers using either standard planar technologies, for example, focused ion beam (FIB)[21,25,28,29], electron-beam lithography (EBL)[30–32], nanoprinting[23,27], or unconventional in-situ approaches, that is, ice lithography[20,26]. However, to date, plasmonic metafibers have predominantly explored separate bare fibres, and little attention has been paid to their practical applications in nonlinear plasmonic regimes[33]. There are also certain challenges for the widespread uptake of metafibers as regular component devices for fibre optics: a) nanofabrication suffers from inevitable mechanical vibrations and thus a poor repeatability of nanostructures due to the large aspect ratio of bare fibres; b) the connections between the functionalised bare fibres and standard optical fibres introduce either potential contaminations and even damage to the plasmonic metasurfaces, for example, through fibre splicing or considerably high insertion losses within the fibre circuit, for example, using fibre optic ferrules. Thus, methods to fabricate metafibers with a reproducible metasurface geometry and standard adapting interfaces are clearly needed.

In this work, we propose methodologies that integrate well-defined metasurfaces directly on the endfaces of commercial single mode fibre jumpers (SMFJs), as shown in Fig. 1a, by using the standard planar technologies. Widely adopted in the fibre-optics community and industry, SMFJs stably hold bare fibres in their central positions with special glues and ceramic pins and reduce external influences, such as bending and vibrations, by using multiple strength jackets. More importantly, they also provide various connection interfaces with ordinary fibre networks, for example, physical contact, ultra-physical contact, and angled physical contact, better depressing the back reflection of the light and thus reducing the return loss. To demonstrate the low insertion loss and practical application in nonlinear plasmonics, metafibers using SMFJs are implemented into fibre laser cavities, serving as special SAs that filter out the quasi-continuous wave (cw) laser background while promoting ultrashort pulse emission within the laser cavity (Fig. 1a). By tuning the plasmonic resonances of the metafibers, we were able to achieve all-fibre sub-picosecond soliton mode-locking at different optical wavelength bands. Finally, insights into the physical mechanisms underlying the saturable absorption of plasmonic metasurfaces are provided.

Results

To pattern plasmonic metasurfaces on the endfaces of commercial SMFJs, the first planar technology we employ is the standard EBL associated with various customised mechanical parts, as shown in Figs. 1b1–b5. An SMFJ (working at 980–1650 nm, FC/PC, Ø900 μm jacket, 1 m long) was cut into two parts from the middle, one of which was stably mounted on a fibre adapter. As illustrated in Fig. 1b1, the fibre adapter could be connected to a rotating chamber designed to fit a commercial spin coater (SUSS MicroTec). After spin-coating the electron-sensitive resist, the rotating chamber was flipped top-down and placed on a hot plate for soft-baking, as shown in Fig. 1b2. The spacing (2.5 mm) between the SMFJ endface and the top surface of the hot plate was guaranteed by the heads of the four screws used to mount the fibre adapter onto the chamber. The fibre adapter was then placed in a commercial scanning electron microscope (SEM, Zeiss Crossbeam 550) for electron beam exposure, owing to a home-built translating chamber mounted on the scanning stage of the SEM, as shown in Fig. 1b3. After exposure and development, the patterned SMFJ was transferred to an evaporator via a home-built evaporation adaptor to deposit the target materials, as illustrated in Fig. 1b4. The final lift-off reveals the metasurface on the fibre endface, concluding the metafiber fabrication process flow. Fig. 1b5 shows a typical metasurface made of a nanorod array fabricated on an SMFJ endface using this technique (see

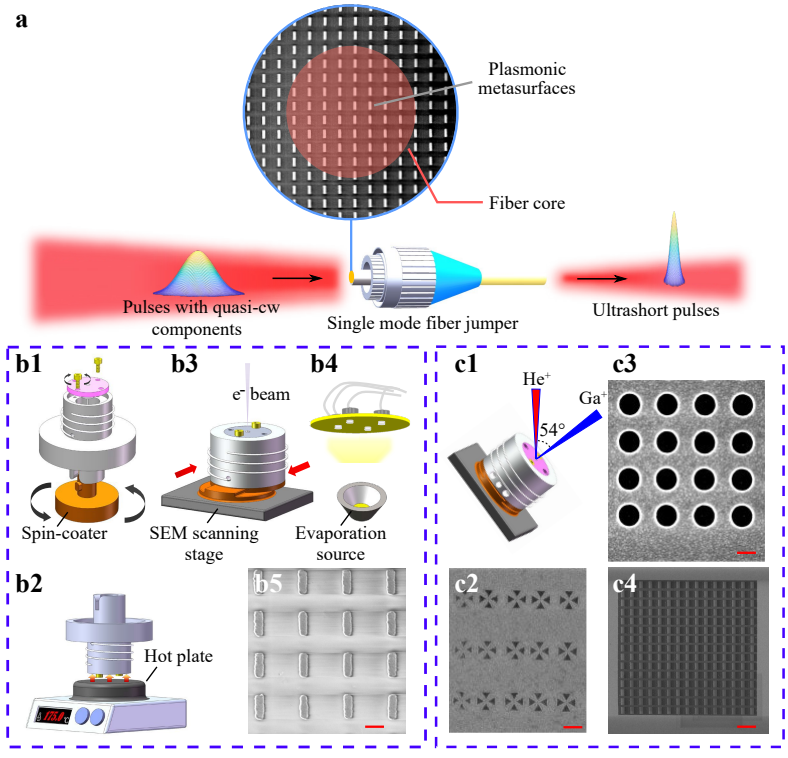

Fig. 1 Nanofabrication of plasmonic metafibers. **a** Schematic of plasmonic metasurfaces integrated on the endface of a standard single mode fibre jumper (SMFJ) used here as saturable absorber (SA) for laser mode locking. **b1**–**b5** Nanofabrication of plasmonic metafibers using standard electron-beam lithography (EBL). **b1** Home-built rotating chamber for the spin-coating of electron-beam resists. **b2** Alternative use of the rotating chamber for the soft-baking. **b3** Translating chamber for the electron-beam exposure. The bottom part is adapted to the scanning stage of a commercial scanning electron microscope (SEM). **b4** SMFJ holder for the physical vapor deposition. **b5** SEM image of an Au nanorod array fabricated on the endface of an SMFJ. The scale bar is 400 nm. The height of the nanostructures is 50 nm. The colour contrast in the substrate is caused by the charge accumulations during the SEM observation. **c1**–**c4** Nanofabrication of plasmonic metafibers using standard focused ion beam (FIB). **c1** Translating chamber for the ion-beam exposure, where He^+ beam is used for imaging and the Ga^+ beam is utilised for milling. The translating chamber is tilted at an angle of 54° in horizontal direction. **c2**–**c4** SEM images of orthogonal Au bow-ties, Au nanoholes, and Au nanorod arrays fabricated on the endface of an SMFJ. The scale bars in **c2**—**c4** represent 1 μm, 400 nm, and 2 μm, respectively. The height of the nanostructures is 60 nm. The horizontal lines connecting two rows of nanorods in **c4** are caused by the charge accumulations during the SEM observations.

'Nanofabrication of the metafiber using EBL' in Supplementary Information for details). The advantages of such methods include low cost and high immunity to complicated plasmonic systems, such as heterodimers[9,34,35].

Alternatively, we also demonstrate the possibility to fabricate plasmonic meta-surfaces on the SMFJ endface using the standard FIB milling, as illustrated in Figs. 1c1–c4. The evaporation adaptor shown in Fig. 1b4 was first used to deposit the target metal, for example, Au. The SMFJ was then transferred to a custom-built translating chamber mounted on the scanning stage of a commercial FIB instrument (Carl Zeiss, ORION NanoFab, Germany) for milling, as shown in Fig. 1c1. Figs. 1c2–c4 shows SEM images of three types of plasmonic metasurfaces on the endfaces of standard SMFJs after milling: orthogonal bowties, nanoholes, and nanorods, respectively (see 'Nanofabrication of the metafiber using FIB' in Supplementary Information for details). Compared to EBL, FIB requires fewer preparation procedures and provides a relatively better resolution for nanopatterning. In addition, because resist spin-coating is not needed, the FIB process flow is compatible with nonplanar fibre interfaces, for example, angled physical contacts, thus offering a fast and convenient way to functionalise most of the commercially available optical fibres.

Thanks to our versatile nanomanufacturing setups, the metasurfaces with specific plasmonic properties can be easily transferred from planar substrates to the fibre endfaces. Thus, we have employed these techniques to fabricate saturable metafibers and then demonstrated their use for laser mode-locking. First, to achieve saturation of optical absorption from a metasurface, we need to tune the

plasmonic resonance to the target wavelength, for example, the C+L telecommunication optical wavebands at 1.5 μm which can be entirely covered simultaneously owing to the broad resonance of the same plasmonic metasurface[15]. Nanorods are one of the most common nanostructures used to achieve designed plasmonic functionalities[15,36]. Indeed, their resonances can be easily tuned from the visible to near-infrared regimes by altering the dimensions of the nanostructures (size and aspect ratios)[15,36]. Fig. 2a shows the theoretical transmission spectra of a 50 nm thin metasurface made of Au nanorods arranged in a square array with a 750 nm period, a constant rod width of 160 nm and varying lengths (see 'Linear optical response calculations' in Supplementary Information for details). The excitation polarisation was parallel to the long axis of nanorods. As shown in Fig. 2a, the metasurface resonated at 1550 nm, which is the central wavelength of the telecommunication band, for a rod length of 470 nm. Such resonance originates directly from the longitudinal dipolar plasmonic mode of the individual nanorods. Based on these numerical calculations, we fabricated the corresponding plasmonic metasurfaces on the endface of a standard SMFJ using EBL, as depicted in Fig. 2b. The measured lengths and widths of the nanorods are 485 nm and 155 nm respectively, with a tolerance of 10 nm. The inset shows the fundamental electric field distribution of a nanorod array with the actual dimensions excited by a plane wave of 1550 nm. The incident polarisation was linear and parallel to the long axis of the nanorods. Strongly confined hotspots can be clearly observed in the near field of the nanorods, as shown in the inset of Fig. 2b, emphasising the excitation of the longitudinal dipolar modes.

To characterise the optical responses, i.e., the resonant absorptions, of the metafibers, a home-built extinction microscope was first employed (see 'Optical setups for measuring the extinction spectra' in Supplementary Information for details). A supercontinuum light source (SLS, NKT photonics) emitting in the 1–1.8 μm spectral range was used to excite the plasmonic metasurfaces. The measured extinction spectra with polarisation dependence

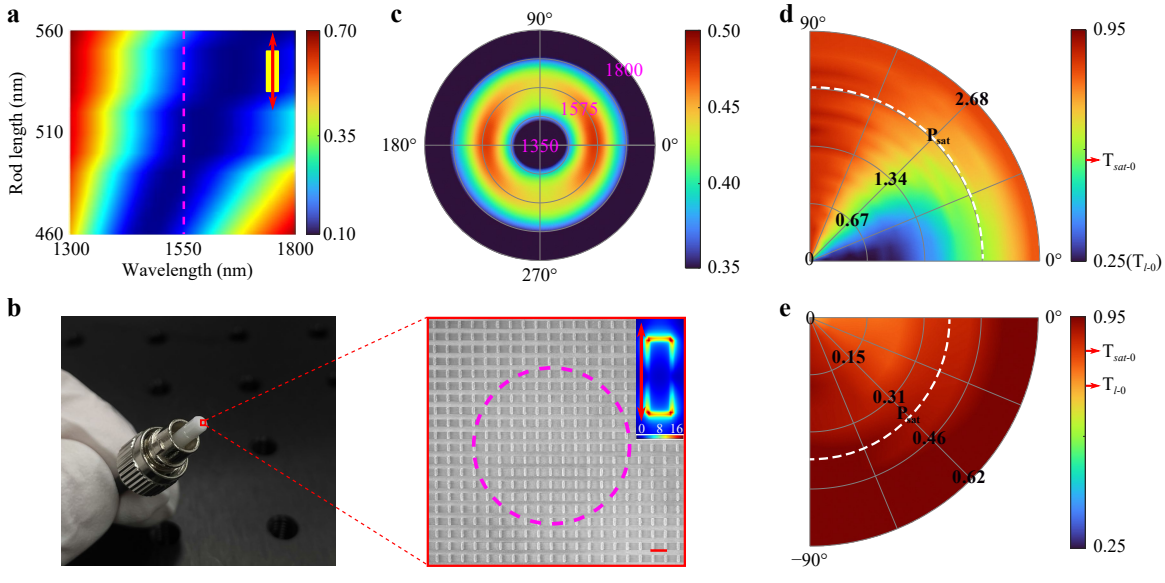

Fig. 2 Nanocharacterisation of the plasmonic metafibers. **a** Calculated transmission spectra of the Au nanorod arrays with varying rod lengths. The rod width is 160 nm and the height is 50 nm. The longitudinal and transverse periods remain constant at 750 nm. The excitation polarisation is parallel to the long axis of the nanorods. The pink dashed line indicates the spectral wavelength of 1550 nm. **b** Photograph of the fabricated metafiber by using EBL and the corresponding SEM image in the fibre core region. The scale bar represents 800 nm. The dashed pink circle indicates the boundary of the fibre core. The inset shows the fundamental electrical field distribution of the nanorod array (taking the periodic conditions into account). The red arrow represents the incident polarisation. The horizontal lines between two rows of nanorods presented in the SEM figure were caused by the charge accumulations during the SEM observations. **c** Experimental polarimetric extinction spectra of the plasmonic metafiber. The polar coordinates (λ,θ) represent the spectral wavelength and the polarisation angle of the incident light. The colour contrast represents the extinction level of the metafiber. **d**, **e** Power- and polarisation-dependent nonlinear transmission of a nanorod array in on-resonance (using 1550 nm fs laser) and off-resonance (using 1950 nm fs laser) excitation conditions. The polar coordinates (P, θ) represent the averaged power in the focus and the polarisation angle of the incident light. The colour contrast represents the transmission level of the nanorod array. The white dashed curves represent averaged saturation powers. $T_{l\text{-}0}$ and $T_{sat\text{-}0}$ denote the transmission levels at θ = 0° in the linear absorption regime and once absorption is saturated, respectively.

are exhibited in Fig. 2c. The polar coordinates (λ, θ) represent the spectral wavelength and incident polarisation angles, respectively. θ = 0° corresponds to incident polarisation parallel to the long axis of the nanorods. The colour contrast represents the extinction level of the metafiber. The extinction spectrum, which denotes the fingerprint of plasmonic resonance, is defined as Ext $(\lambda) = [T_{ref}(\lambda) - T_{nr}(\lambda)]/T_{ref}(\lambda)$, where $T_{ref}(\lambda)$ is the transmission of the reference fibre, $T_{nr}(\lambda)$ is the transmission of the metafiber, and λ is the wavelength. The reference fibre is identical to the metafiber except that there are no plasmonic nanostructures on the endface. The dipole radiation-like map demonstrates the dominant role of the longitudinal dipolar mode of the metasurfaces. The plasmonic resonances are generally located at 1550 nm and have an average full width at half maximum (FWHM) of 200 nm. Depending on the excitation polarisation, the extinction fluctuates in an approximate sine/cosine function.

Following the linear optical characterisation, nanorod metasurfaces with the same patterns are fabricated on a glass substrate with the same refraction index as the SMF core by using standard EBL, in order to further investigate their power- and polarisation-dependent nonlinear optical responses. The nonlinear transmittance was measured using a home-built optical setup with an ultrashort pulsed pumping laser (see 'Optical setups for measuring nonlinear optical transmissions' in Supplementary Information for details). The repetition rate of the laser was 10.32 KHz and the output wavelength was tuned from 600 nm to 2400 nm via an optical parametric amplifier. The pulse duration varied slightly with the output wavelength, for example, it changed from 179 fs to 166 fs as the wavelength was tuned from 1550 nm to 1950 nm. The incident polarisation was linear and thus the polarisation axis with respect to the nanorod orientation was tuned with a half-waveplate. Using this laser, we recorded the transmission of the nanorod array under study and used the transmission of a nearby blank glass slide as a reference.

We first used the excitation laser at the central wavelength of 1550 nm, where the plasmonic resonance of the nanorod array locates. The result is plotted in the polar pseudocolour diagram shown in Fig. 2d, in which the polar coordinates (P, θ) represent the average power in the focus and the input polarisation angle, and the colour map represents the transmission level of the array. θ ranges from 0° to 90° with respect to the long axis of the nanorods. With this representation, saturable absorption with power and polarisation dependencies appears clearly. At lower power, the transmission of the nanorod array remains constant, T_l, for a given polarisation. In this linear regime, the transmission strongly depends on the incident polarisation because T_l is inversely proportional to the absorption cross section of the nanorod. Above a critical power, the overall transmission increases nonlinearly until it reaches a saturated value T_{sat}, indicating saturation of the metasurface absorption. For all the input polarisation orientations, the power-dependent transmission coefficient shows a 'S'-shape profile, from which the modulation depth, saturation intensity P_{sat}, and the parameters of T_l and T_{sat} could be obtained by fitting the data (see 'Laser intensity dependent optical transmission model' in Supplementary Information for details). The modulation depth shows a strong dependence on the incident polarisation, ranging from 5% to 57% when the polarisation is tuned from the short axis to the long axis of nanorods. Such high modulation depths exceed the best performance of 2D-SAs[37]. When the same nanorod metasurface was excited with a 1950 nm pulsed laser, a clear decrease in the polarisation dependency was observed, as shown in Fig. 2e. This lowering of the polarisation dependency also results in global growth of the transmission at a minimum of 70% and a drop in the modulation depth at a maximum of 26%. The mismatch between the plasmonic resonance and fundamental excitation significantly reduces the linear and nonlinear absorptions of the nanorod array, resulting in an unremarkable saturable absorption. The results in Fig. 2d, e can probably explain why considerably low modulation depths were reported previously on colloidal Au nanorods, as the dispersed sizes and orientations averaged the saturable absorption and the critical contribution of plasmonic resonances[14,17,18].

The saturable absorption can be helpful for achieving the formation of ultrashort pulses in laser architectures, ultimately reaching self-starting passively mode-locked regimes[15]. To further test the fabricated samples and provide a practical demonstration of the saturable metasurfaces application in nonlinear optics, metafibers were integrated into the fibre laser cavities to promote mode locking. The fibre cavity shown in Fig. 3 was constructed, which included a 980 nm pump diode (LD, maximum pump power of 88 mW), a 980/1550 nm wavelength multiplexer (WDM), 35 cm of erbium-doped fibre (EDF, Nufern, SM-ESF-7/125), a polarisation-insensitive isolator (ISO), a polarisation controller (PC), and an output fibre coupler (OFC). The PC is used to alter the laser polarisation in the cavity, targeting a proper SA efficiency by virtue of the polarimetric properties of the metafibers shown in Fig. 2c, d. The coupler extracts 10% of the laser energy for pulse characterisation. The overall length of the cavity is 8.8 m with anomalous net chromatic

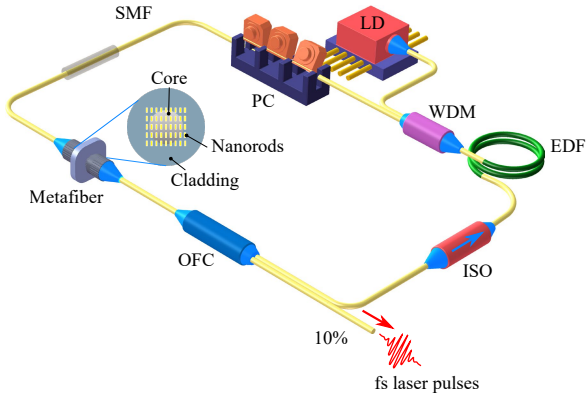

Fig. 3 Home-built ultrafast fibre laser integrating a plasmonic metafiber, where LD represents the pump laser diode, WDM is the wavelength-division multiplexer, EDF is the erbium-doped fibre, ISO is the optical isolator, OFC is the output fibre coupler, SMF stands for standard single-mode telecom fibre, and PC is the polarisation controller.

dispersion, and all the fibre connections are made with a standard telecom fibre SMF-28e.

In such an overall anomalous dispersion regime, the chromatic dispersion and the self-phase modulation accumulated during a cavity roundtrip can balance on average, preventing a significant pulse broadening and leading to a so-called optical soliton regime[38]. The output pulse train and radio frequency (RF) spectra were monitored using an oscilloscope (Tektronix, 1 GS/s, 100 MHz) and RF spectrum analyser (Keysight, N9000B), respectively. The pulse spectra, output power, and autocorrelation trace were monitored using an optical spectrum analyser (Yokogawa, AQ6375), a power meter (Thorlabs, S148C), and an autocorrelator (FR-103XL), respectively. Fig. 4a shows the average laser output power featuring a CW laser conversion efficiency of 5.5% without the metafiber SA, noting that the conversion efficiency is limited by the moderate 10% output coupling. The laser threshold was approximately 13 mW, demonstrating the relatively low loss of the entire cavity. After the implementation of the metafiber SA into the laser cavity, the power threshold of the CW laser increased to 23 mW owing to the insertion loss. We note the low mode-locking threshold at a pump power of 38 mW, and the conversion efficiency of the mode-locked laser is reduced to 1.8%, resulting from an efficient laser regime discrimination performed by the metafiber SA. Fig. 4b shows the optical spectrum of the laser mode-locked with the metafiber SA for a pump power of 49 mW. The

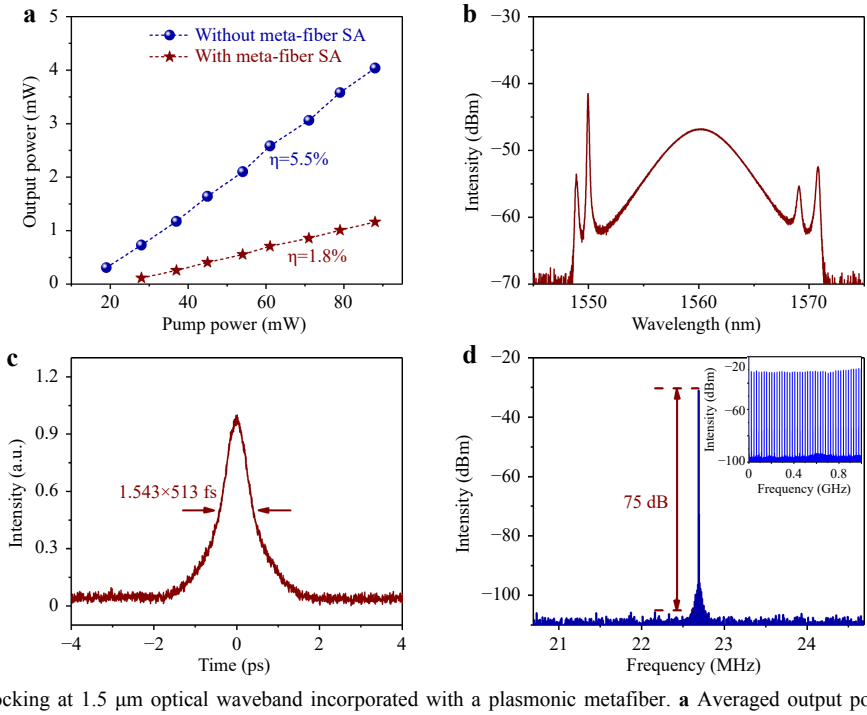

Fig. 4 Soliton mode-locking at 1.5 μm optical waveband incorporated with a plasmonic metafiber. **a** Averaged output power of a mode-locked fibre laser with the metafiber SA (red stars) and a cw laser without the metafiber SA (blue dots) as functions of the pump power. **b** Soliton pulse spectrum at pump power of 49 mW. **c** Autocorrelation trace of a single soliton at pump power of 58 mW. **d** RF spectrum of the soliton pulses with a scanning range of 5 MHz and a resolution of 300 Hz. The inset shows the RF spectrum of the soliton pulses with a scanning range of 1 GHz and a resolution of 10 KHz.

spectrum has a smooth broadband central part with a 3-dB bandwidth of 6 nm, centred at 1560 nm. Two sets of Gordon–Kelly sidebands appear on both sides of the spectrum, which is a typical feature of fibre lasers mode-locked in the vector soliton regime[39–41]. Fig. 4c shows the optical autocorrelation trace at a pump power of 58 mW. A pulse duration of 513 fs was inferred from the measurement, and the time-bandwidth product (TBP) was estimated to be 0.379, indicating that the output pulses were slightly chirped, as compared with the expected TBP of 0.315 for an unchirped exact hyperbolic-secant-shaped pulse[38]. The time interval between subsequent output pulses was measured to be 44 ns, which corresponds to the fundamental frequency of 22.7 MHz in Fig. 4d. Fig. 4d presents the RF spectra of the soliton mode-locked pulse at a pump power of 58 mW. The signal-to-noise ratio of the fundamental frequency of the laser can reach 75 dB at a resolution of 300 Hz, and the signal-to-noise ratio of the RF spectrum in the range of 0–1 GHz is greater than 60 dB at a resolution of 10 KHz, indicating remarkably high stability of the laser pulses.

The soliton pulses can be tuned to other optical wavelength bands, e.g., 2 μm in a thulium fibre laser, by adapting the plasmonic resonance of a metafiber to the gain spectrum of the laser cavity. To achieve resonant absorption at 2 μm for example, we use similar nanorod metasurfaces but with different landscapes. As shown in Fig. 5a, the transmission spectra of nanorod arrays with constant width (340 nm) and spacings (longitudinal and transverse periods: 1 μm) but different lengths were calculated. The rod length can be evaluated as 680 nm, where the longitudinal dipolar mode of the plasmonic metasurfaces is located at 2 μm. Guided by the numerical predictions, we fabricated corresponding plasmonic metasurfaces on an SMFJ endface using FIB, as shown in the SEM image in Fig. 5b. The longitudinal and transverse periods remained the same at 1 μm. The length and width of the nanorods were measured as 690 nm and 345 nm with

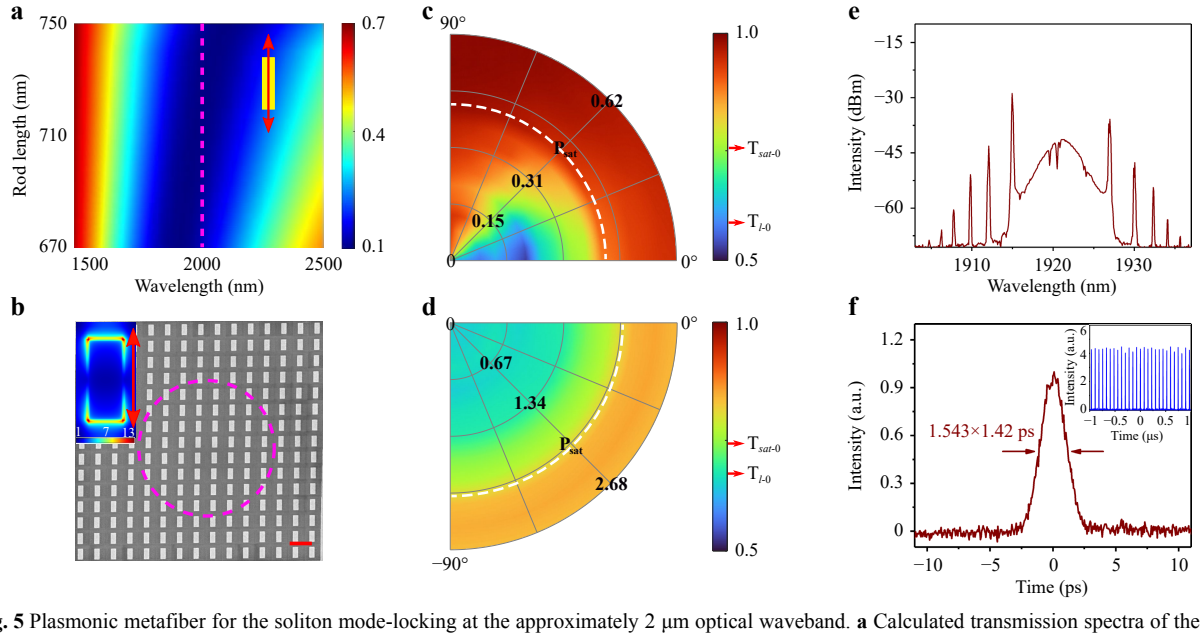

Fig. 5 Plasmonic metafiber for the soliton mode-locking at the approximately 2 μm optical waveband. **a** Calculated transmission spectra of the Au nanorod metasurfaces with varying rod lengths. The rod width is 340 nm. The longitudinal and transverse periods are maintained constant as 1 μm. The excitation polarisation is parallel to the long axis of the nanorods. The height of the nanostructures is set to 60 nm. The pink dashed line indicates the spectral wavelength of 2 μm. **b** SEM image of an Au nanorod metasurface fabricated on the endface of a standard SMFJ by using FIB. The length and width of the nanorods are 690 nm and 345 nm with a tolerance of 10 nm, respectively. The longitudinal and transverse periods are the same: 1 μm. The height of the nanostructures is 60 nm. The scale bar represents 1 μm. The dashed pink circle indicates the boundary of the fibre core. The inset shows the fundamental electrical field distribution of the nanorod array (taking periodic conditions into account). The red arrow in the inset indicates the input polarisation. **c**, **d** Power- and polarisation-dependent nonlinear transmission of a nanorod array in on-resonance (using 1950 nm fs laser) and off-resonance (using 1550 nm fs laser) excitation conditions. The polar coordinates (P, θ) represent the averaged power in the focus and input polarisation, respectively. The colour contrast represents the transmission level of the nanorod array. The white dashed curves represent averaged saturation powers. $T_{l\text{-}0}$ and $T_{sat\text{-}0}$ denote the transmission levels at the initial states of linear absorption and saturable absorption when $\theta = 0°$, respectively. **e** Soliton pulse spectrum generated by a thulium-doped fibre laser incorporating a metafiber SA, at the pump power of 310 mW. **f** Autocorrelation trace of a single soliton at the pump power of 310 mW. The inset shows the pulse trains over a longer time range (2 μs). The time interval is 72 ns.

a tolerance of 10 nm, respectively. The inset shows the fundamental electric field distribution of a nanorod array with actual dimensions excited by a linearly polarised plane wave at 2 μm. The nonlinear transmission spectra with incident power and polarisation-dependencies are measured in both the on-resonance and off-resonance cases, similar to Fig. 2c, d. In the on-resonance case, fs-pulsed laser with a central wavelength of 1950 nm was used as the light excitation source (Fig. 5c), whereas in the off-resonance case, the wavelength of the excitation laser was switched to 1550 nm (Fig. 5d). Similarly, strong polarimetric linear and nonlinear absorption can be clearly observed from the former, while the polarisation dependency almost disappears for the latter. The maximum modulation depth in the former case was 37%, whereas it decreased to 18% for the latter. The metafiber was then placed into a laser cavity operating in the 2 μm region, which resulted in stable soliton mode-locking (see 'Soliton mode-locking at 2 μm' in Supplementary Information for details). The time-averaged pulse spectrum is shown in Fig. 5e at the pump power of 310 mW, featuring multiple pairs of symmetric sidebands. The central wavelength was 1921.1 nm, and the FWHM of the spectrum was 3.2 nm. Fig. 5f exhibits the pulse autocorrelation trace and pulse trains at a pump power of 310 mW. The pulse duration of 1.42 ps is measured.

It is notable here that we have not managed to reach any mode-locked regime in the off-resonance cases (as shown in Fig. 2f and Fig. 5d), demonstrating the unambiguous roles of plasmonic resonances in the saturation absorption and promotion of laser mode-locking. We also observed no visible thermal damage from such metafiber SAs following their usage in ultrafast pulse generation (for both the 1.5 μm and 2 μm cases), even at the maximum pump powers, indicating the good thermal conductivity and stability of the plasmonic metasurfaces against optical damage (see 'Thermal damage threshold estimation' in Supplementary Information for details).

The low mode locking threshold is a clear signature of the high efficiency of our designed plasmonic metasurfaces as SAs offering high contrast and limited insertion losses. However, we note a possible contribution of virtual saturable absorption owing to the nonlinear polarisation evolution in optical fibres, which is known to favour mode locking in fibre laser cavities in the presence of polarisation-dependent losses[42]. Such a possible interplay will be the subject of subsequent investigation.

Discussion

For the first time, we achieved highly stable soliton mode-locking at different optical wavebands, promoted by plasmonic metasurfaces directly patterned on the fibre facets. Considering the previous work on solid-state SAs, such as semiconductor saturable absorber mirrors[43], our metafiber SAs allow for more cost-effective, timesaving, broadband, and tunable nonlinear absorption compatible with all-fibre operation for ultrashort pulse generation and reshaping[15,44]. In addition, because of the short hot-carrier relaxation dynamics arising from a plasmonic system, the pulse duration from a metafiber laser can easily reach a typical sub-picosecond time scale, in contrast to the situation with common semiconductors having relaxation times of several picoseconds[8,45,46]. Compared with widely investigated low-dimensional materials, including graphene[37], graphene oxide[47], carbon nanotubes[48], black phosphorus[49], transition metal dichalcogenides[50–53], topological insulators[54,55], and colloidal nanoparticles[14,17,18], in addition to fully competitive or superior performance on saturable absorption and laser mode-locking (Fig. 6a), the remarkable properties reported here mainly originate from the plasmonic nature of the metasurfaces themselves. Indeed, the plasmonic modes of metasurfaces, which are highly size-, shape-, and orientation-dependent, are fully guaranteed by highly resolved nanofabrication techniques originating from planar technologies. Therefore, the resonance wavelength and polarimetric properties of metasurfaces can be quantitatively tuned through design. This will allow the metasurfaces to reach an extraordinarily high modulation depth that is still compatible with a relatively low pump threshold for promoting mode-locked regimes. The merits of plasmonic metasurfaces compared to other 2D materials with dispersed sizes and random orientations are illustrated in Fig. 6a. A large modulation depth leads to reliable self-starting owing to the strong pulse shaping performed by SAs[56]. A low mode-locking threshold is also particularly beneficial to achieve in the second step, harmonic mode-locking, which multiplies the laser output repetition rate[52]. Considering the pioneering works using plasmonic metasurfaces as SAs in a free-space coupled laser cavity[15], our metafiber will allow a straightforward implementation within standard fibre networks, targeting an ultracompact fibre laser and optical pulse reshaper, as well as other 'all-in-fibre' optical systems.

As material-based SAs have become one of the key elements for a fibre laser architecture to achieve stable passive mode locking, it is worth clarifying the physical mechanisms related to the saturable absorption of plasmonic metasurfaces. Below, we propose several principles from both macroscopic and microscopic points of view to better interpret the physical nature, as the classical absorption and transmission models used in SAs

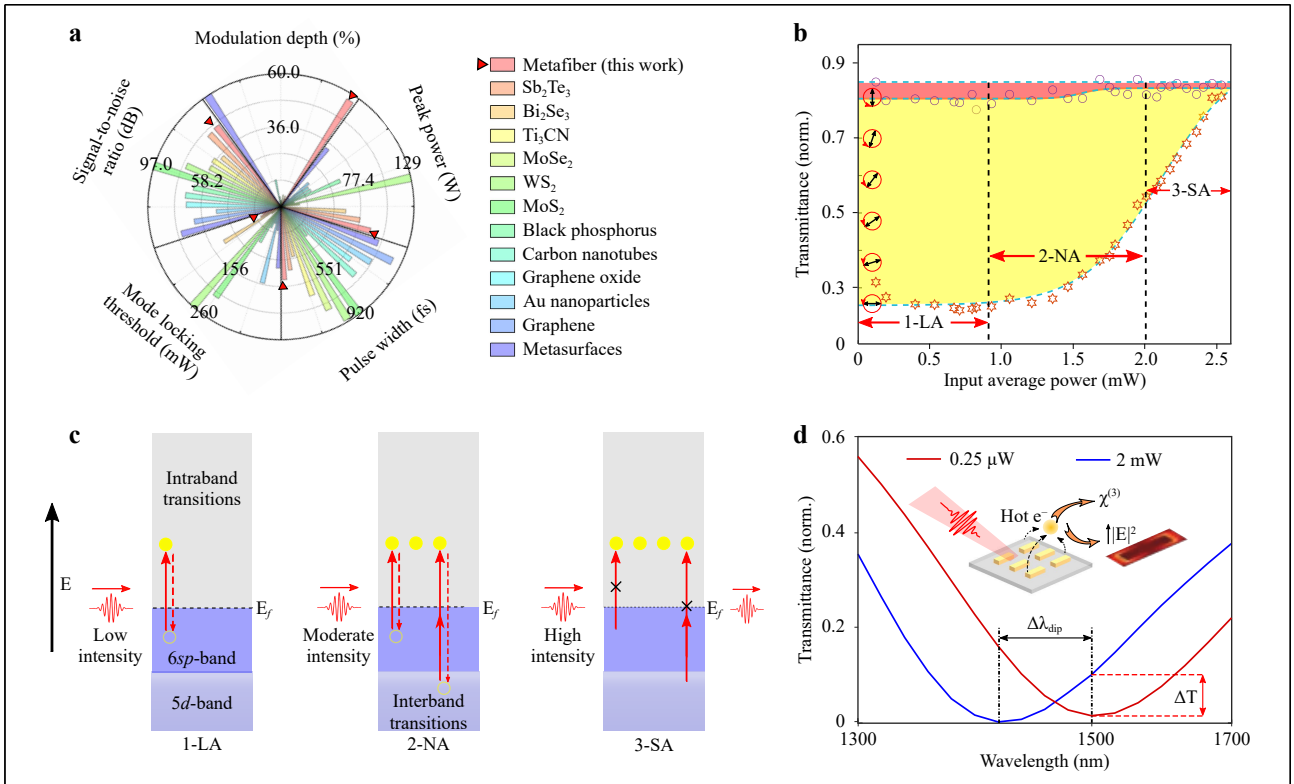

Fig. 6 Laser performance comparisons and saturable absorption mechanisms for the metafiber SAs. **a** Performance comparisons of soliton mode-locking lasers at 1.5 μm optical waveband using different material SAs. The metafiber SA is highlighted with red triangles. **b** Power- and polarisation-dependent saturation process of plasmonic metasurfaces. Three stages leading to the saturation absorptions are distinguished in accordance with the pumping laser power: linear absorption (LA), nonlinear absorption (NA), and saturation absorption (SA). Two contributors are involved depending on the excitation polarisation for each stage: bulk material effect (filled with red) and surface plasmon effect (filled with yellow). The opened stars and circles are the raw transmission data from Fig. 2e for the polarisation angles 0° and 90° with respect to the long axis of nanorods, respectively. The dashed cyan lines are the corresponding fitted data. The black arrows indicate the excitation polarisations. **c** Saturation absorption mechanism from the aspect of the bulk material effect. Carrier transitions occur at given high density-of-states symmetry points of energy bands as the input power increases. The closed yellow circles stand for the electrons and the opened circles are the holes left. The solid and dashed arrows represent the excitation and relaxation processes, respectively. **d** Saturation absorption mechanism from the aspect of surface plasmon effect. Surface plasmon induced nonlinearity shifts the absorption resonance ($\Delta\lambda_{dip}$) and modifies the transmission level (ΔT) of a plasmonic SA. The red and blue lines represent the transmission spectra of a nanorod metasurface excited with an averaged input power of 0.25 μW and 2 mW in a fs laser focus, respectively.

basically treat bulk semiconductor materials. First, it is essential to note the intrinsic differences between the bulk and nanoscale materials. As the size decreases to the nanoscale, the properties of atoms present on the outer boundary of the particles become dominant[57]. The optical properties change significantly in comparison with those of the bulk owing to their size-dependent interactions with light. This works for in particular plasmonic metasurfaces, which rely on the surface plasmon resonances contributed by collective conduction electron oscillations[8]. Following this principle, the saturable absorption of plasmonic metasurfaces can generally be divided into two contributors: the bulk material effect and the surface plasmon effect. As illustrated in Fig. 6b, the former (filled with red colour) can be extracted from a special 'off-resonance excitation' test, in which the excitation polarisation is perpendicular to the long axis of the nanorods. In such circumstances, the longitudinal dipolar plasmon mode of the metasurfaces, which plays a dominant role in the unusual polarimetric linear and nonlinear optics performance, is almost entirely depressed. As can be observed from Fig. 6b, the transmission remains at a global high level (>80%) and is almost immune to increasing input power. The saturation process induced by bulk metal materials can still be described by the classical energy band theory. The reason stems from the physical fact that there are forbidden bands at some high density-of-states symmetry points for noble metals, e.g., X or L points in the first Brillouin zone of gold[58,59], where most of the carrier transitions take place in a light excitation[8,60]. As

shown in Fig. 6b, c, the entire absorption process with increasing pumping power can generally be divided into three stages: linear absorption, nonlinear absorption, and saturable absorption. We note here that the launch of the next step does not simultaneously quit the previous steps. In the linear absorption stage, as depicted in Fig. 6c, the sp electrons below the Fermi level E_f are excited to states above E_f through intraband transitions. The excited electrons relax to the sp bands and recombine with the holes left at a sub-picosecond timescale[61,62]. In the ultrafast pumping regime, that is, when the pulse duration of the pumping laser is shorter than the relaxation time of hot electrons, the electrons from the d bands can also be excited to the state above E_f through interband transitions, inducing multiphoton absorption[8,59,60], for example, two-photon absorption, as depicted in Fig. 6c. This nonlinear absorption gradually dominates as the pumping intensity increases. When the pumping intensity becomes sufficiently high, the photogenerated carrier population increases significantly and occupies all the states in the conduction bands, which blocks further absorption owing to the Pauli exclusion principle, leading to saturated absorption of plasmonic metasurfaces[45,63].

Next, we thoroughly discuss the surface plasmon effect, which contributes to the majority of saturable absorption for the plasmonic metasurfaces, as shown in the yellow region in Fig. 6b. Surface plasmons can be interpreted as playing a two-fold role in accordance with the light–matter interaction formula: $P(\omega) = \varepsilon_0\chi^{(1)}E(\omega)+\varepsilon_0(\chi^{(2)}E(\omega)^2+\chi^{(3)}E(\omega)^3+...)$, where ε_0 is the permittivity of free space, and $\chi^{(1)}$, $\chi^{(2)}$, and $\chi^{(3)}$ are the first three terms of susceptibilities[64]. As illustrated in the inset of Fig. 6d, the surface plasmons provide a dramatic local field enhancement for the electric field E, especially when their resonances match the fundamental or high-order harmonic excitation frequencies[9,65,66]. Furthermore, the surface components of nonlinear susceptibilities, for example, $\chi^{(3)}_{surf}$ in the process of two-photon absorption, will be significantly altered owing to the hot carrier redistributions during strong light–matter interactions[35,45,46,67]. Given the above two contributions, an extra hot carrier (mainly from electrons)-induced nonlinearity is produced and shifts the absorption resonances[67]. As shown in Fig. 6d, considering an increase in input power from 0.25 μW to 2 mW, the plasmonic resonance initially designed at 1550 nm was shifted to 1457 nm and the transmission level showed an increase of 8.5% (see 'Optical nonlinearity induced plasmonic resonance shift' in Supplementary Information for details). Thus, the strong dependencies on the pumping laser power and polarisation for the transient transmission of plasmonic metasurfaces are another key origin of the saturated absorption.

In conclusion, we report on a nanomanufacturing method to integrate plasmonic metasurfaces directly on the fibre endfaces of commercial SMFs and a first demonstration of their applications in nonlinear plasmonics regime. In contrast to the metasurfaces solely on bare fibres that most of the current studies consider, our approach treats SMFs or more general multi-mode fibres with universal adapting interfaces, yielding advantages of compatibility with fibre networks and robustness against external influences such as bending and mechanical vibrations. In addition, because only standard nanofabrication techniques are involved, the process flow can be accessed by worldwide cleanrooms. By featuring various plug-and-play connections, low insertion loss, and cost-effective nanofabrication, metafibers with functionalised plasmonic properties could potentially become a new regular fibre component in the fibre optics community. To demonstrate a practical application, the metafibers were implemented in multiple fibre laser cavities, acting as special SAs to assist lasers in mode lock. The results show that the metafiber SAs have unique features, including broad absorption spectra, tunable plasmonic resonances, high modulation depth, and ultrafast recovery time, which are competitive with the best performance of state-of-the-art 2D materials. All-fibre sub-picosecond mode-locked laser pulses were generated in 1.5 μm and 2 μm regions. The application of such SAs can be immediately extended to other optical wavebands by tuning the plasmonic resonances of metafibers. As such, saturable plasmonic metafibers provide ultrathin SAs for applications where tunable nonlinear transfer functions are needed, such as in ultrafast lasers, pulse shaping, and regeneration, and have become key enablers for compact and efficient optical frequency combs or neuromorphic circuits. The work enriches the 'lab-on-fibre' paradigm and offers an avenue to realise the 'all-in-fibre' optical systems.

Materials and methods

Method All of the details about the nanofabrication, extinction simulations, linear and nonlinear optical characterisations, saturation absorption model, soliton mode locking at 2 μm, damage threshold test on the plasmonic metafibers, and optical nonlinearity induced plasmonic resonance shift are provided in Supplementary Information.

Acknowledgements
The authors gratefully acknowledge funds from the National Natural Science Foundation of China (61927820, 51806199, 61905200), the

National Key Research and Development Program of China (2017YFA0205700) and Natural Science Fundation of Zhejiang Province (LR21E020005). J. Wang thanks Dr. Ziyang Zhang from the School of Engineering, Westlake University, for the technical support with the fibre setups. J. Wang, L. Zhang, B. Chen, and Q. Jia thank the Westlake Center for Micro/Nano Fabrication for facility support and technical assistance.

Author details

[1]College of Information Science and Electronic Engineering, Zhejiang University, Hangzhou 310027, China. [2]Key Laboratory of 3D Micro/Nano Fabrication and Characterization of Zhejiang Province, School of Engineering, Westlake University, 18 Shilongshan Road, Hangzhou 310024, Zhejiang Province, China. [3]Institute of Advanced Technology, Westlake Institute for Advanced Study, 18 Shilongshan Road, Hangzhou 310024, Zhejiang Province, China. [4]Laboratory of Infrared Material and Devices & Key Laboratory of Photoelectric Materials and Devices of Zhejiang Province, Advanced Technology Research Institute, Ningbo University, Ningbo 315211, China. [5]Laboratoire Interdisciplinaire Carnot de Bourgogne, UMR 6303 Université Bourgogne Franche-Comté, 9 avenue Alain Savary, 21078 Dijon, France. [6]Interdisciplinary Center for Quantum Information and Department of Physics, Zhejiang University, Hangzhou, China. [7]College of Information Science and Electronic Engineering, Zhejiang University, Hangzhou 310027, China. [8]School of Materials Science and Engineering, Zhejiang University, Hangzhou 310027, China. [9]State Key Laboratory of Modern Optical Instrumentation, College of Optical Science and Engineering, Zhejiang University, Hangzhou 310027, China

Author contributions

All the authors contributed extensively to the work presented in this paper. M. Qiu and J. Wang conducted the research project. B. Cluzel, A. Coillet, P. Grelu, J. Wang, and M. Qiu conceived the main conceptual ideas. J. Wang and L. Zhang developed methodologies to fabricate metafibers. D. Wu and X. Shen supervised the work on the fibre laser mode-locking. L. Zhang, Q. Jia, and B. Chen prepared samples. L. Zhang, N. Tang, F. Liu, X. Sun, H. Yu, F. Qiu, X. Liu, and J. Qiu contributed to the linear and nonlinear optical characterisation. H. Zhang and X. Chen conducted fibre-laser mode-locking experiments. J. Wang, L. Ying, W. Yan, W. E. I. Sha, L. Zhang, and M. Qiu proposed the principles of the saturation absorption mechanisms. All authors contributed to the discussion and writing of the manuscript. L. Zhang and H. Zhang contributed equally to this work.

Conflict of interest

The authors declare that they have no conflicts of interest.

Supplementary information is available for this paper at https://doi.org/10.37188/lam.2022.045.

Received: 25 March 2022 Revised: 11 May 2022 Accepted: 23 May 2022
Accepted article preview online: 26 July 2022

References

1. Shelby, R. A., Smith, D. R. & Schultz, S. Experimental verification of a negative index of refraction. *Science* **292**, 77-79 (2001).
2. Schurig, D. et al. Metamaterial electromagnetic cloak at microwave frequencies. *Science* **314**, 977-980 (2006).
3. Sun, S. L. et al. Gradient-index meta-surfaces as a bridge linking propagating waves and surface waves. *Nature Materials* **11**, 426-431 (2012).
4. Yu, N. F. & Capasso, F. Flat optics with designer metasurfaces. *Nature Materials* **13**, 139-150 (2014).
5. Maier, S. A. Plasmonics: Fundamentals and Applications. (New York: Springer, 2007).
6. Geng, J. et al. Controllable generation of large-scale highly regular gratings on Si films. *Light: Advanced Manufacturing* **2**, 274-282 (2021).
7. Krasnok, A., Tymchenko, M. & Alù, A. Nonlinear metasurfaces: a paradigm shift in nonlinear optics. *Materials Today* **21**, 8-21 (2018).
8. Wang, J. Y. et al. Carrier recombination and plasmonic emission channels in metallic photoluminescence. *Nanoscale* **10**, 8240-8245 (2018).
9. Wang, J. Y. et al. Strong second-harmonic generation from Au-Al heterodimers. *Nanoscale* **11**, 23475-23481 (2019).
10. Zhao, Y., Yang, Y. M. & Sun, H. B. Nonlinear meta-optics towards applications. *PhotoniX* **2**, 3 (2021).
11. Goi, E. et al. Perspective on photonic memristive neuromorphic computing. *PhotoniX* **1**, 3 (2020).
12. Kumar, S., Williams, R. S. & Wang, Z. W. Third-order nanocircuit elements for neuromorphic engineering. *Nature* **585**, 518-523 (2020).
13. Shastri, B. J. et al. Photonics for artificial intelligence and neuromorphic computing. *Nature Photonics* **15**, 102-114 (2021).
14. Kang, Z. et al. Passively mode-locking induced by gold nanorods in erbium-doped fiber lasers. *Applied Physics Letters* **103**, 041105 (2013).
15. Wang, J. Y. et al. Saturable plasmonic metasurfaces for laser mode locking. *Light: Science & Applications* **9**, 50 (2020).
16. Zhao, D. et al. Plasmonic saturable absorbers. *Advanced Photonics Research* **2**, 2100003 (2021).
17. Wang, X. D. et al. Microfiber-based gold nanorods as saturable absorber for femtosecond pulse generation in a fiber laser. *Applied Physics Letters* **105**, 161107 (2014).
18. Shu, Y. Q. et al. Gold nanorods as saturable absorber for harmonic soliton molecules generation. *Frontiers in Chemistry* **7**, 715 (2019).
19. Han, A. P. et al. Nanopatterning on nonplanar and fragile substrates with ice resists. *Nano Letters* **12**, 1018-1021 (2012).
20. Hong, Y. et al. Three-dimensional in situ electron-beam lithography using water ice. *Nano Letters* **18**, 5036-5041 (2018).
21. Principe, M. et al. Optical fiber meta-tips. *Light: Science & Applications* **6**, e16226 (2017).
22. Xiong, Y. F. & Xu, F. Multifunctional integration on optical fiber tips: challenges and opportunities. *Advanced Photonics* **2**, 064001 (2020).
23. Plidschun, M. et al. Ultrahigh numerical aperture meta-fibre for flexible optical trapping. *Light: Science & Applications* **10**, 57 (2021).
24. Umakoshi, T., Saito, Y. & Verma, P. Highly efficient plasmonic tip design for plasmon nanofocusing in near-field optical microscopy. *Nanoscale* **8**, 5634-5640 (2016).
25. Consales, M. et al. Metasurface-enhanced lab-on-fiber biosensors. *Laser & Photonics Reviews* **14**, 2000180 (2020).
26. Hong, Y. et al. Solvent-free nanofabrication based on ice-assisted electron-beam lithography. *Nano Letters* **20**, 8841-8846 (2020).
27. Zou, M. Q. et al. Fiber-tip polymer clamped-beam probe for high-sensitivity nanoforce measurements. *Light: Science & Applications* **10**, 171 (2021).
28. Savinov, V. & Zheludev, N. I. High-quality metamaterial dispersive grating on the facet of an optical fiber. *Applied Physics Letters* **111**, 091106 (2017).
29. Martins, T. et al. Fiber-integrated phase change metasurfaces with switchable group delay dispersion. *Advanced Optical Materials* **9**, 2100803 (2021).
30. Consales, M. et al. Lab-on-fiber technology: toward multifunctional optical nanoprobes. *ACS Nano* **6**, 3163-3170 (2012).
31. Wang, N. et al. Boosting light collection efficiency of optical fibers using metallic nanostructures. *ACS Photonics* **6**, 691-698 (2019).
32. Yermakov, O. et al. Nanostructure-empowered efficient coupling of light into optical fibers at extraordinarily large angles. *ACS Photonics* **7**,

2834-2841 (2020).
33. Xu, J. et al. Second harmonic generation in amorphous silicon-on-silica metamaterial. *APL Photonics* **6**, 036110 (2021).
34. Horneber, A. et al. Compositional-asymmetry influenced non-linear optical processes of plasmonic nanoparticle dimers. *Physical Chemistry Chemical Physics* **15**, 8031-8034 (2013).
35. Wang, J. Y. et al. Hot carrier-mediated avalanche multiphoton photoluminescence from coupled Au-Al nanoantennas. *Journal of Chemical Physics* **154**, 074701 (2021).
36. Sun, Y. G. & Xia, Y. N. Shape-controlled synthesis of gold and silver nanoparticles. *Science* **298**, 2176-2179 (2002).
37. Fu, B. et al. Broadband graphene saturable absorber for pulsed fiber lasers at 1, 1.5, and 2 μm. *IEEE Journal of Selected Topics in Quantum Electronics* **20**, 1100705 (2014).
38. Agrawal, G. P. Fiber-Optic Communication Systems. 4th edn. (New York: Wiley, 2010).
39. Kelly, S. M. J. Characteristic sideband instability of periodically amplified average soliton. *Electronics Letters* **28**, 806-807 (1992).
40. Zhao, L. M. et al. Soliton trapping in fiber lasers. *Optics Express* **16**, 9528-9533 (2008).
41. Wang, Y. T. et al. Nonlinear Fourier transform enabled eigenvalue spectrum investigation for fiber laser radiation. *Photonics Research* **9**, 08001531 (2021).
42. Li, G. M. et al. Passive mode locking resulting from weak polarization dependence based on evanescent field interaction with a monolayer graphene absorber. *Applied Optics* **57**, 3507-3510 (2018).
43. Keller, U. Recent developments in compact ultrafast lasers. *Nature* **424**, 831-838 (2003).
44. Liu, W. J. et al. Tungsten disulphide for ultrashort pulse generation in all-fiber lasers. *Nanoscale* **9**, 5806-5811 (2017).
45. Del Fatti, N. et al. Nonequilibrium electron dynamics in noble metals. *Physical Review B* **61**, 16956-16966 (2000).
46. Baida, H. et al. Ultrafast nonlinear optical response of a single gold nanorod near its surface Plasmon resonance. *Physical Review Letters* **107**, 057402 (2011).
47. Boguslawski, J. et al. Graphene oxide paper as a saturable absorber for Er- and tm-doped fiber lasers. *Photonics Research* **3**, 119-124 (2015).
48. Wang, F. et al. Wideband-tuneable, nanotube mode-locked, fibre laser. *Nature Nanotechnology* **3**, 738-742 (2008).
49. Sotor, J. et al. Black phosphorus saturable absorber for ultrashort pulse generation. *Applied Physics Letters* **107**, 051108 (2015).
50. Wu, K. et al. 463-MHz fundamental mode-locked fiber laser based on few-layer MoS_2 saturable absorber. *Optics Letters* **40**, 1374-1377 (2015).
51. Wu, K. et al. WS_2 as a saturable absorber for ultrafast photonic applications of mode-locked and Q-switched lasers. *Optics Express* **23**, 11453-11461 (2015).
52. Koo, J. et al. Femtosecond harmonic mode-locking of a fiber laser at 3.27 GHz using a bulk-like, $MoSe_2$-based saturable absorber. *Optics Express* **24**, 10575-10589 (2016).
53. Jhon, Y. I. et al. Metallic MXene saturable absorber for femtosecond mode-locked lasers. *Advanced Materials* **29**, 1702496 (2017).
54. Boguslawski, J. et al. Mode-locked Er-doped fiber laser based on liquid phase exfoliated Sb_2Te_3 topological insulator. *Laser Physics* **24**, 105111 (2014).
55. Li, K. X. et al. L-band femtosecond fibre laser based on Bi_2Se_3 topological insulator. *Laser Physics Letters* **12**, 105103 (2015).
56. Cheng, L. et al. Linear and nonlinear optical properties modulation of Sb_2Te_3/*GeTe* bilayer film as a promising saturable absorber. *Results in Physics* **13**, 102282 (2019).
57. Pareek, V. et al. Synthesis and applications of noble metal nanoparticles: a review. *Advanced Science*, *Engineering and Medicine* **9**, 527-544 (2017).
58. Guerrisi, M., Rosei, R. & Winsemius, P. Splitting of the interband absorption edge in Au. *Physical Review B* **12**, 557-563 (1975).
59. Boyd, G. T., Yu, Z. H. & Shen, Y. R. Photoinduced luminescence from the noble metals and its enhancement on roughened surfaces. *Physical Review B* **33**, 7923-7936 (1986).
60. Imura, K., Nagahara, T. & Okamoto, H. Near-field two-photon-induced photoluminescence from single gold nanorods and imaging of Plasmon modes. *The Journal of Physical Chemistry B* **109**, 13214-13220 (2005).
61. Hohlfeld, J. et al. Electron and lattice dynamics following optical excitation of metals. *Chemical Physics* **251**, 237-258 (2000).
62. Wang, J. Y. et al. Direct comparison of second harmonic generation and two-photon photoluminescence from single connected gold nanodimers. *The Journal of Physical Chemistry C* **120**, 17699-17710 (2016).
63. Schröder, W. U. et al. Effect of Pauli blocking on exchange and dissipation mechanisms operating in heavy-ion reactions. *Physical Review Letters* **44**, 308-312 (1980).
64. Boyd, R. W. Nonlinear Optics. 3rd edn. (New York: Academic Press, 2008).
65. Thyagarajan, K., Butet, J. & Martin, O. J. F. Augmenting second harmonic generation using fano resonances in plasmonic systems. *Nano Letters* **13**, 1847-1851 (2013).
66. Ren, M. L. et al. Giant enhancement of second harmonic generation by engineering double plasmonic resonances at nanoscale. *Optics Express* **22**, 28653-28661 (2014).
67. Hache, F. et al. The optical Kerr effect in small metal particles and metal colloids: the case of gold. *Applied Physics A* **47**, 347-357 (1988).